

A single cell-based model of the ductal tumour microarchitecture

KATARZYNA A. REJNIAK^{†*} and ROBERT H. DILLON[‡]

[†]Division of Mathematics, University of Dundee, Dundee DD1 4HN, Scotland, UK

[‡]Department of Mathematics, Washington State University, Pullman, WA 99164, USA

(Received 21 August 2006; revised 11 February 2007; in final form 16 February 2007)

The preinvasive intraductal tumours, such as the breast or prostate carcinomas, develop in many different architectural forms. There are, however, no experimental models explaining why cancer cells grow in these various configurations. We use a mathematical model to compare different proliferative conditions that can lead to such distinct microarchitectures. In order to simulate different scenarios of tumour growth, we employed a single cell-based technique that allows us to model development of the whole tumour tissue by focusing on biomechanical processes of individual cells and on communication between cells and their microenvironment. Formation of four specific intraductal tumour patterns, micropapillary, cribriform, tufting and solid, are presented in this paper together with a discussion on gradual dedifferentiation of ductal epithelial cells that gives rise to these distinct carcinomas. We introduce two versions of our cell-based model to show that the obtained results do not depend on a particularly chosen cell structure.

Keywords: DCIS; Tumour growth; Immersed boundary method; Single cell model

AMS Subject Classification: 76D05; 76Z99; 92C37; 92C50

1. Introduction

Medical diagnoses of tumour progression and prognoses of clinical outcomes depend, in part, on recognizing morphologic alterations of tumoural cells and tissues and their cytological abnormalities. The preinvasive intraductal tumours arising from the epithelial tissues (such as the breast ductal carcinomas *in situ*: DCIS or the prostate intraepithelial neoplasias: PIN) develop in many different architectural forms, including solid, comedo, cribriform, micropapillary, flat, trabecular or tufting patterns, to name the most commonly observed by pathologists. Several different histological patterns have been already described ([1,2,8,9,19,20]). Histological grading systems, such as the Gleason score for the prostate carcinomas and the Van Nuys grading system for the breast carcinomas reflect a combination of predisposing genetic changes and acquired abnormalities, and are used to classify tumours and to provide prognostic information to guide the adequate clinical treatment. The low histological “score” is assigned to tumoural tissues containing many well differentiated cells that correspond to tumours in the transition zone and of a low malignant potential; whereas a high “score” is assigned to tissues that consists of poorly differentiated cells showing their progressive invasive potential [2,9].

*Corresponding author. Email: rejniak@maths.dundee.ac.uk

Little is known about how the genotypic abnormalities associated with cancers actually lead to the histological phenotypes observed in carcinomas *in vivo* [3,9]. There are a few mouse models of human and murine prostate or breast ductal tumours, that display some of the morphological features of the various human DCIS [12,17]. However, in most cases the mixed tumour patterns are detectable in the same histological samples and they are relatively untractable for studying cell-biological processes and signalling pathways involved in oncogenic transformations [3]. We are aware of only one model *in vitro* [18] which shows the disruption of cell polarity that results in the structure containing multiple small and incomplete lumens resembling the cribriform pattern. However, new experimental systems for studying other types of DCIS may be available in a near future due to increasing interest in 3D models of normal epithelial acini that are successively grown in culture [3,10,11]. Lack of experimental *in vitro* models which allow one to monitor formation of various tumour forms and to explain why cancer cells grow in these distinct patterns leads to a situation when pathologists must rely on finding lesions with intermediate appearances in order to investigate how various histologic patterns develop. This reduces cancer diagnosis to pattern recognition only, instead of finding the carcinogenic mechanisms.

Normal epithelia lining breast or prostate ducts form one-layered sheets of cells that are anchored to basal membranes and serve as highly selective barriers. Thus the morphology of epithelial cells and all their processes are tightly coordinated. The cells maintain an apico-basal polarity and specialized cell-cell contacts. Moreover, the orientation of cell mitosis is controlled in such a manner as to maintain the normal tissue architecture and structural integrity. It is known that normal epithelial breast cells can acquire two specific orientations of the nuclear spindle and thus two planes of cytokinesis. The cell division perpendicular to the lumen results in two lumenally-positioned daughter cells and leads to the duct outgrowth. The cell division parallel to the lumen gives rise to one lumenally- and one basally-positioned daughter cell, and culminates in the basal cell differentiation into a myoepithelial cell or its apoptosis [6,7]. Ductal carcinomas originate from the epithelial cells; however, as the tumour growth progresses, the tumoural cells lose their epithelial characteristics. Due to certain mutations, tumour cells can escape the highly controlled mechanisms of cell growth and death observed in the epithelium. This leads to the overgrowth of ductal cells known as a hyperplasia and then to various forms of ductal carcinomas. Histological patterns of four specific intraductal tumours, micropapillary, cribriform, tufting and solid, are shown in figure 1. We want to focus our attention on these four microarchitectures to propose a hypothesis that these tumour patterns can be ordered according to changes in the epithelial characteristics of their precursor cells. Our goal is to use a mathematical model to compare different proliferative conditions that can lead to such distinct growth patterns. Such criteria may include increasing the cell growth rate or modifying the orientation of cell division. In order to simulate different scenarios of tumour growth, we have employed a single cell-based technique that allows us to model development of the whole tumour tissue by focusing on biomechanical processes of individual cells and on communication between cells and their environment. We present here two implementations of this cell-based approach that give qualitatively similar results in simulating the development of various patterns of intraductal microarchitectures. The use of these two different implementations shows that the obtained patterns are not artefacts of the model cell structure.

The rest of the paper is organized as follows. The mathematical framework of the cell-based model is introduced in section 2. Computational simulations of different intraductal microarchitectures using both implementations of our model are presented in section 3.

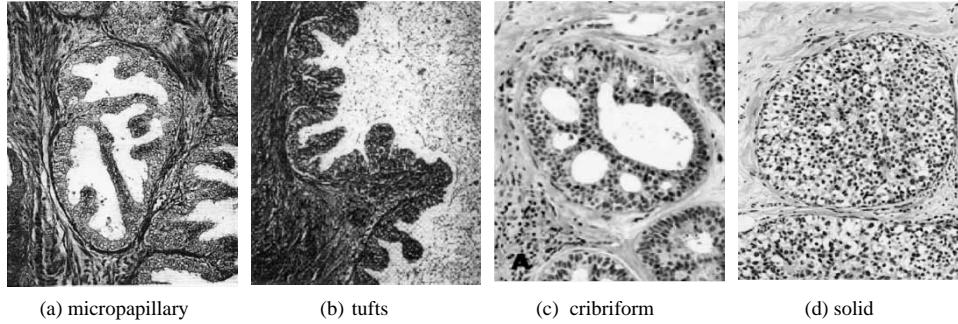


Figure 1. Histological patterns of four ductal carcinomas: (a) micropapillary with trabecular bars, (b) tufts (both in the prostate tissue, from Ref. [1]), (c) cribriform, and (d) solid (both in the breast tissue, from Ref. [20]).

Section 4 contains final conclusions and discussion. Both implementations are described in detail in Appendix A.

2. Outline of the mathematical model

Our mathematical model is based on the immersed boundary method [13] and couples mechanics of elastic bodies (here: cells) with the dynamics of the viscous incompressible fluid (here: the cytoplasm and the extracellular matrix). The main advantage of this method is that it allows the introduction of a variable number of cells, each of arbitrary shape. In addition, each cell is treated as a separate entity with individually regulated cell processes, such as cell growth, division, senescence, adhesion and communication with other cells and with the environment.

2.1. A general framework for a cell-based model

Each cell in our model is treated as an individual body consisting of its own elastic plasma membrane modelled as a network of linear springs and the fluid cytoplasm that provides the cell mass. Interactions between the elastic cells and the viscous incompressible fluid are traced using the immersed boundary method. The cell cycle is regulated independently for each individual cell, but separate cells can interact with other cells and with the environment via a set of discrete cell membrane receptors located on the cell boundary. In particular, the adhesion between distinct cells and between cells and the basal membrane is modelled by introducing adhesive–repulsive forces that act between boundaries of two distinct bodies. The growth of a cell is achieved by placing sources and sinks of fluid inside and outside the host cell to model the transport of fluid across the cell membrane. This creates a flow that pushes on a boundary of the growing cell and increases its area (figure 2a,b). Those sources and sinks are deactivated when the cell area is doubled. Cell division is modelled by introducing contractile forces acting on opposite sides of the cell boundary that results in splitting the host cell into two daughter cells (figure 2c,d).

The fluid is described on a fixed Eulerian lattice $\mathbf{x} = (x_1, x_2)$ in the whole domain Ω , and the configuration Γ_i of the membrane of the i th cell is defined in the curvilinear coordinates $\mathbf{X}_i(l, t)$, where l is a position along the cell boundary. The no-slip condition of a viscous fluid implies that the material boundary points of cell boundaries are carried along with the fluid at

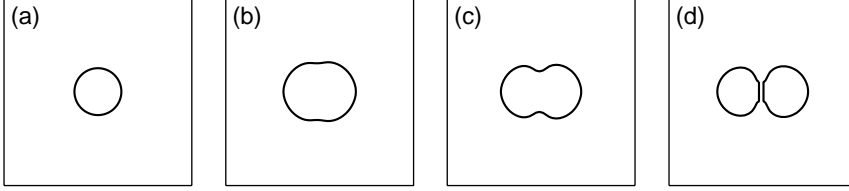


Figure 2. Main phases of the cell cycle: (a) cell ready to proliferate, (b) cell growth and elongation, (c) formation of the contractile ring, and (d) cellular division and formation of two daughter cells.

the local fluid velocity,

$$\frac{\partial \mathbf{X}_i(l, t)}{\partial t} = \mathbf{u}(\mathbf{X}_i(l, t), t) = \int_{\Omega} \mathbf{u}(\mathbf{x}, t) \delta(\mathbf{x} - \mathbf{X}_i(l, t)) d\mathbf{x}. \quad (1)$$

A force density $\mathbf{F}_i(l, t)$ defined at each boundary point contains adjacent forces $\mathbf{F}_{\text{adj}(i)}(l, t)$ arising from elastic properties of the cell membrane, contractile forces $\mathbf{F}_{\text{div}(i)}(l, t)$ acting during the division of a host cell into two daughter cells and adhesive forces $\mathbf{F}_{\text{adh}(i)}(l, t)$ that define connections with other cells and with the basal membrane,

$$\mathbf{F}_i(l, t) = \mathbf{F}_{\text{adj}(i)}(l, t) + \mathbf{F}_{\text{div}(i)}(l, t) + \mathbf{F}_{\text{adh}(i)}(l, t).$$

This force is applied directly to the fluid in the δ -layer region around the boundary Γ_i of the i th cell, where δ is a two-dimensional Dirac delta function: $\delta(\mathbf{x}) = \delta(x_1)\delta(x_2)$,

$$\mathbf{f}_i(\mathbf{x}, t) = \int_{\Gamma_i} \mathbf{F}_i(l, t) \delta(\mathbf{x} - \mathbf{X}_i(l, t)) dl. \quad (2)$$

The growth of the i th cell is achieved by placing discrete collections Ξ_i^p of point sources ($p = +$) and point sinks ($p = -$) inside and outside the cell, respectively. This source-sink configuration models transport of the fluid through the cell membrane in such a way, that fluid introduced in all internal sources \mathbf{Y}_k^+ is balanced by the loss of fluid in the external sinks \mathbf{Y}_k^- for each cell separately. These source and sink contributions are transmitted to the surrounding fluid using the Dirac delta function,

$$s_i(\mathbf{x}, t) = \sum_{k \in \Xi_i^+} S^+(\mathbf{Y}_k^+, t) \delta(\mathbf{x} - \mathbf{Y}_k^+) + \sum_{k \in \Xi_i^-} S^-(\mathbf{Y}_k^-, t) \delta(\mathbf{x} - \mathbf{Y}_k^-). \quad (3)$$

The initial configuration of our system represents a circular cross section through the duct, as shown in figure 3. It contains one layer of epithelial cells located along the duct. These cells are initially identical, but the tumour growth is initiated in some of them. The layer of epithelial cells is surrounded by a stiff circular basal membrane, that supports growth of tumours inside the lumen of the duct. The whole domain is filled with a viscous incompressible fluid.

A configuration Γ_{BM} of the basal membrane is defined in a very similar way by using the curvilinear coordinates $\mathbf{Z}(l, t)$, where l is a position along the basal membrane. Its stiff properties arise from adjacent $\mathbf{F}_{\text{adj}}(l, t)$ and tethered forces $\mathbf{F}_{\text{tet}}(l, t)$ that keep the shape of the basal membrane intact and immobile. Connections between the basal membrane and the epithelial cells are defined by adhesive forces $\mathbf{F}_{\text{adh}}(l, t)$. These three kinds of forces constitute

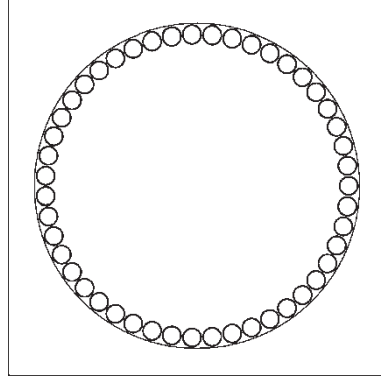


Figure 3. Initial configuration of the system consists of several identical cells arranged in one layer along the duct and surrounded by the basal membrane. The duct inside is completely filled with lumen. All intraepithelial tumours will be initiated in some of the epithelial cells along the duct.

the force density $\mathbf{F}_{\text{BM}}(l, t)$ that is transmitted to the fluid in the δ -layer region around the basal membrane. The boundary points move also at the local fluid velocity; however, due to the tethered forces a dislocation of the basal membrane is insignificant. Equations describing the behaviour of the basal membrane are summarized as follows,

$$\mathbf{F}_{\text{BM}}(l, t) = \mathbf{F}_{\text{adj}}(l, t) + \mathbf{F}_{\text{tet}}(l, t) + \mathbf{F}_{\text{adh}}(l, t),$$

$$\mathbf{f}_{\text{BM}}(\mathbf{x}, t) = \int_{\Gamma_{\text{BM}}} \mathbf{F}_{\text{BM}}(l, t) \delta(\mathbf{x} - \mathbf{Z}(l, t)) dl, \quad (4)$$

$$\frac{\partial \mathbf{Z}(l, t)}{\partial t} = \mathbf{u}(\mathbf{Z}(l, t), t) = \int_{\Omega} \mathbf{u}(\mathbf{x}, t) \delta(\mathbf{x} - \mathbf{Z}(l, t)) d\mathbf{x}. \quad (5)$$

We assume that the density ρ and viscosity μ of the fluid $\mathbf{u}(\mathbf{x}, t)$ are constant, and that the fluid motion is governed by the Navier–Stokes equations:

$$\rho \left(\frac{\partial \mathbf{u}}{\partial t} + (\mathbf{u} \cdot \nabla) \mathbf{u} \right) = -\nabla p + \mu \Delta \mathbf{u} + \frac{\mu}{3\rho} \nabla s + \mathbf{f}. \quad (6)$$

where $p(\mathbf{x}, t)$ is the fluid pressure, the external force $\mathbf{f}(\mathbf{x}, t)$ is defined at the boundaries of all cells and the basal membrane:

$$\mathbf{f}(\mathbf{x}, t) = \sum_i \mathbf{f}_i(\mathbf{x}, t) + \mathbf{f}_{\text{BM}}(\mathbf{x}, t),$$

and the source-sink distribution $s(\mathbf{x}, t)$ is taken around all growing cells: $s(\mathbf{x}, t) = \sum_i s_i(\mathbf{x}, t)$.

The continuity equation with a source term describes the mass balance law, where the source distribution s is identically equal to zero on the whole fluid domain except at the isolated point sources and sinks around the growing cells:

$$\rho \nabla \cdot \mathbf{u} = s(\mathbf{x}, t). \quad (7)$$

It is required, however, that the conservation of mass is preserved globally in the fluid domain Ω at each time t , *i.e.*

$$\int_{\Omega} s(\mathbf{x}, t) d\mathbf{x} = \rho \int_{\Omega} \nabla \cdot \mathbf{u}(\mathbf{x}, t) d\mathbf{x} = 0$$

2.2. Numerical algorithm

In order to implement our models numerically, we discretise the fluid domain Ω using a uniform square grid with a constant mesh width h . Similarly, the cell membranes and the basal membrane are represented by Lagrangian points \mathbf{X}_l and \mathbf{Z}_l , respectively, both with boundary points separation of $\Delta l \approx h/2$. The computation proceeds in time steps of duration Δt . For convenience we use the superscript notation, that is $\mathbf{u}^n(\mathbf{x}) = \mathbf{u}(\mathbf{x}, n\Delta t)$. At the end of time step n the fluid velocity field \mathbf{u}^n and the configuration of the boundary points \mathbf{X}^n and \mathbf{Z}^n are known. These values are updated at the next time step in the following way:

- i) Determine the source-sink distribution S^n at points \mathbf{Y}_k locating around all growing cells; spread these values to the neighbouring grid points to find the local expansion rate s^n of the fluid.
- ii) Calculate the total force density \mathbf{F}^n from the configuration of the cell boundary points and the basal membrane; spread those values to the neighbouring grid points to determine the forces \mathbf{f}^n acting on the fluid.
- iii) Solve the Navier–Stokes equations for the fluid velocity field \mathbf{u}^{n+1} by using the fast Fourier transform algorithm with periodic boundary conditions imposed on the fluid domain.
- iv) Interpolate the fluid velocity field \mathbf{u}^{n+1} to each immersed boundary point and compute their new positions \mathbf{X}^{n+1} and \mathbf{Z}^{n+1} by moving them at the local fluid velocity.

The Navier–Stokes equations (6) and (7) are discretised using the first order finite difference scheme with the spatial difference operators: forward D^+ , backward D^- , center D^0 and upwind D^\pm ($r = 1, 2$ denotes the first and second vector field components, respectively):

$$\begin{cases} \rho \left(\frac{u_r^{n+1} - u_r^n}{\Delta t} + \sum_{s=1}^2 u_s^n D_s^\pm u_r^n \right) = -D_r^0 p^{n+1} + \mu \sum_{s=1}^2 D_s^+ D_s^- u_r^{n+1} + \frac{\mu}{3\rho} D_r^0 s^n + f_r^n, \\ \rho \sum_{s=1}^2 D_s^0 u_s^{n+1} = s^n. \end{cases} \quad (8)$$

Equations (1)–(5) are discretised as follows:

$$\begin{aligned} s^n(\mathbf{x}) &= \sum_k S^n(\mathbf{Y}_k) \delta_h(\mathbf{x} - \mathbf{Y}_k), \\ \mathbf{f}^n(\mathbf{x}) &= \sum_l \mathbf{F}^n(\mathbf{X}_l) \delta_h(\mathbf{x} - \mathbf{X}_l) \Delta l, \\ \mathbf{u}^{n+1}(\mathbf{X}) &= \sum_{ij} \mathbf{u}^{n+1}(\mathbf{x}_{ij}) \delta_h(\mathbf{x}_{ij} - \mathbf{X}) h^2, \\ \mathbf{X}^{n+1} &= \mathbf{X}^n + \Delta t \cdot \mathbf{u}^{n+1}(\mathbf{X}). \end{aligned} \quad (9)$$

Interactions between the fluid grid and the material points are implemented using the discrete approximation $\delta_h(\mathbf{x})$ to the Dirac delta function, where $\delta_h(\mathbf{x}) = \delta_h(x_1) \cdot \delta_h(x_2)$ and

$$\delta_h(r) = \begin{cases} \frac{1}{4h} \left(1 + \cos\left(\frac{\pi r}{2h}\right)\right) & \text{if } |r| < 2h, \\ 0 & \text{if } |r| \geq 2h. \end{cases} \quad (10)$$

More details about the numerical implementation of this algorithm and the numerical solution of the Navier–Stokes equations can be found in Refs [4,14].

2.3. Two implementations of the cell-based model

The presented description of a cell-based model using the immersed boundary framework is quite general and gives some freedom in defining certain elements of the model. We use in this paper two versions of this general method that differ in the design of the cell membrane structure, in the location of sources and sinks of the fluid around the growing cells, and in selection of the mitotic orientation during the cell division. In the model used by KAR, the cell membrane is represented by one closed curve and each boundary point on this curve is connected to its four neighbours (two on each side) by short linear springs. In the growing cell a single source of fluid is located at the cell centroid and several balancing sinks are placed outside the cell boundary. The orientation of cell division is chosen either orthogonal to the cell’s longest axis or orthogonal to the cell boundary that adheres to other cells. In the model used by RHD, the cell membrane consists of two closed curves that are interconnected by a mesh of short linear springs. In the growing cell the pairs of fluid sources and sinks are placed along the cell boundary in the form of discrete channels. The axis of cell division is chosen either randomly or it is approximately orthogonal to the (normal) line running from the cell centroid to the closest point on the basal membrane.

These differences between our two model implementations reflect trade-offs between computational cost and biological realism. Defining the cell boundary as a spring network will give the cell more rigidity, but each additional spring connection leads to an increase of computational costs since additional boundary forces need to be computed in each step of the algorithm. Both, however, allow for cell deformability and interactions with other cells. The source-sink distributions used in both our implementations are simplifications of the real process of cell growth, but they both result in similar expansion of the area of the growing cell. However, the membrane water channels used for the fluid transport during the cell growth are more faithfully represented by the source-sink doublets located along the cell boundary. It is not known how real cells select their axis of cell division, and we presented here a few different algorithms that lead to the effects observable in nature. However, the assumption of using only local information (the shape of the dividing cell and local cell–cell adhesion) for selecting the mitotic axis seems to be more realistic biologically. More details about both implementations and the specific forms of various forces and source-sink distributions used in all simulations are discussed in Appendix A.

By using two different implementations of our cell-based model we show that the presented microarchitectural patterns do not depend on the details of the cells’ model structure, but are the result of cellular properties and cell–cell interactions. It is also worthwhile to point out here, that by using two versions of the general modelling approach that produce comparable results, we show the potential of our single cell-based technique in modelling various patterns of the multicellular growth, simultaneously giving the modeller a

certain degree of freedom in defining some model details. This allows the modeller to find a balance between the true representation of biological structures and the computational costs needed for simulations. In fact, versions of this mathematical framework have been used before by each author to model deformations of the trophoblast bilayer [14], the development of avascular tumours [15,16], and the growth of multicellular organisms [5].

3. Computational results

Due to the lack of experimental models that would be able to trace the development of ductal carcinomas, we can rely only on comparison between histological samples of normal tissues and those that present fully developed tumours. In order to address mechanisms that lead to distinct geometrical patterns of ductal carcinomas, all our simulations start from the configuration of a normal duct. Tumoural growth is initiated in some epithelial cells around the duct and the tumour is traced until it reaches a fully developed pattern. We focus our attention on four tumour microarchitectures: micropapillary, cribriform, tufting and solid. Histologically they all are characterized by maintaining an intact layer of epithelial cells in contact with the uninterrupted basal membrane. Intraluminal proliferations occur in all four cases, but with different degrees of lumen filling.

Computational simulations of the morphological development of all four patterns are presented below. To show that the final results do not depend on a particularly chosen model cell structure, the tufting and solid patterns have been simulated using both implementations of our model. For each case we start with a short description of the morphological pattern of real tumours, as seen in biopsy samples collected by pathologists and described in the cited papers. Our simulations focus entirely on biomechanical processes of individual cells and on interactions between cells that lead collectively to the desired tumour morphology. Differences between separate patterns have been achieved by varying only two proliferative conditions of tumour cells: (i) the orientation of cell division, and (ii) the cell replication potential. Limited variability of the planes of cell division due to synchronized cell epithelial polarisation and suppression of cell growth leading to cell senescence after producing only a few offspring are both hallmarks of a strong epithelial characteristics. In contrast, the unbounded cell proliferation and lack of cell polarity that leads to random orientation of cell division is characteristic for aggressive tumours. Therefore, our choice of these two proliferative conditions allows for comparison of all four patterns taking into account a minimal number of features that differentiate between normal and tumoural cells.

3.1. Micropapillary pattern

The micropapillary pattern shown in figure 1a, called also the “clinging carcinoma”, consists of numerous fronds protruding into the lumen. They may vary in their appearance from short projections, to long slender finger-like structures extending across the lumen. Some of them span only short peripheral sections of the duct forming epithelial arches, so-called “Roman bridges”; others can extend across the duct to form trabecular bars or to intersect randomly in a form of the lacework (compare [1,20]). That leads some pathologists to group micropapillary and cribriform lesions together. We differentiate here between these two patterns assuming that if the intraductal structure is composed of two layers of cells only, it is classified as micropapillary. Four snapshots from the corresponding simulation by KAR are shown in figure 4. Here, the cell growth is initiated in six cells spread uniformly along the

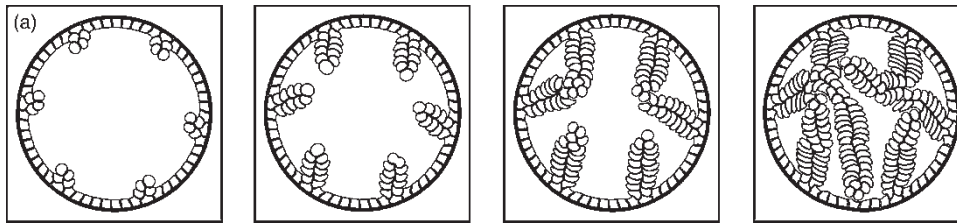


Figure 4. Development of the micropapillary pattern initiated from six epithelial cells spread uniformly along the duct. Four representative snapshots from the simulation of KAR are shown.

duct. The final pattern has been achieved by rare proliferations of the most intraductal cells only and by imposing the same orientation in all cell divisions. All tumoural cells have a very limited duplicability and all of them, except the most intraductal, are quiescent. The orientation of cell division is determined identically for all dividing cells and is orthogonal to the plane of adhesion with other cells. This leads to a very slow outgrowth of long slender fronds that finally form the lacework by accidental intersections. Location and number of initial sides of tumour cells are chosen such that it is possible to observe that the growing tumour clones cross each other. In real ducts the micropapillary fronds can be located in a more variable way.

3.2. Cribriform pattern

An example of the cribriform pattern is shown in figure 1c. It is characterized by the formation of multiple microlumens located randomly inside the ducts and surrounded by tumour cells. The microlumens have regular roundish shapes. The intraductal cells have similar growth properties regardless of their location within the duct that suggests their monoclonal characteristics (compare [8,20]). The corresponding computational simulation by RHD is shown in figure 5. Progression in the development of the cribriform microarchitecture is shown in four snapshots, beginning with its initiation in six ductal cells and ending with the fully developed pattern. The final result has been achieved by imposing identical rules for determining the orientation of cell division. All cells split in the direction orthogonal to the line running from the cell centroid to the closest point on the basal membrane. This leads to the finger-like structures that grow faster into the lumen than in their width, and finally intersect to form multiple lumens. Location and number of initial sides of tumour cells are chosen such that it is possible to observe that the growing tumour clones join with their neighbours; however, in real ducts the microlumens can be of more variable sizes and can be located in a more random fashion.

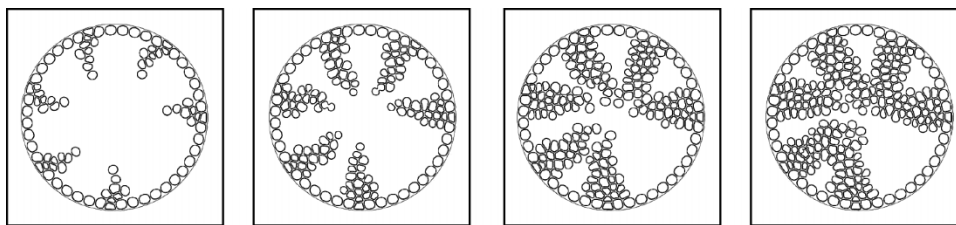


Figure 5. Development of the cribriform pattern initiated from six epithelial cells spread uniformly along the duct. Four representative snapshots from the simulation of RHD are shown.

3.3 Tufting pattern

Tufting patterns shown in figure 1b have been observed mostly in the prostate. They appear as stratified mounds and heaps of cells protruding into the lumens, reaching only a few layers in width. It is characteristic that these tufts are quite evenly spaced around the ducts, but they do not extend across the lumen [1,19]. The corresponding computational simulations shown in figure 6a,b have been produced by reduced cell proliferation with random orientation of cell divisions. Therefore, the cells forming the tufting patterns exhibit limited ability for growing inside the lumen and lack of cell polarisation. Progression in the development of this pattern obtained by using both implementations of our cell-based model are shown in figure 6a,b. Both simulations start with initiation of the cell growth in six uniformly spread cells and they both end when the tufting pattern is fully developed. Differences in the shapes of tufts arising in both simulations are a result of differently defined algorithms for determining the orientation of cell division, but nevertheless both final configurations of tufts are similar. In the model of RHD, the mitotic orientation is chosen randomly, which results in more finger-like shapes of tufts. In the model of KAR, the preferred direction of cell division is roughly orthogonal to the plane of cell adhesion with their neighbours, if the cell is not surrounded by other cells. Alternatively, the cell divides orthogonally to its longest axis. This results in more compact shapes of tufts.

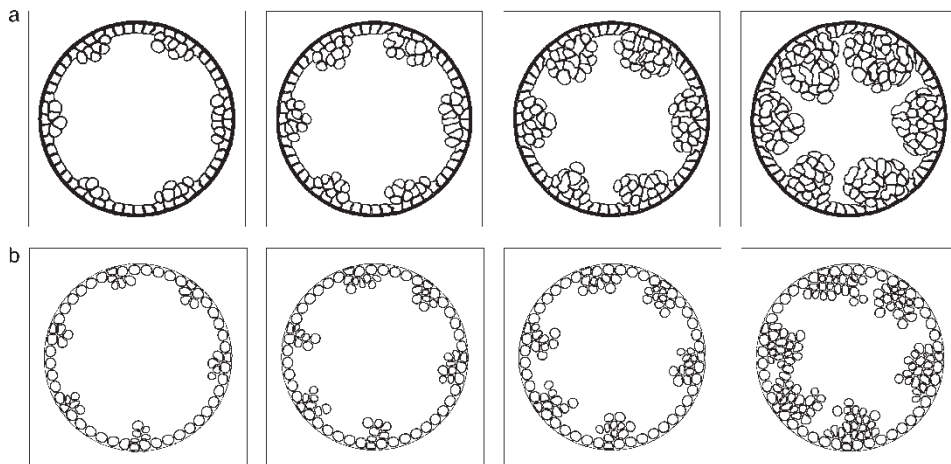


Figure 6. Development of the tufting pattern initiated from six epithelial cells spread uniformly along the duct. Four representative snapshots from simulations of KAR (upper row) and RHD (bottom row) are shown.

3.4. Solid pattern

An example of the solid tumour is shown in figure 1d. Solid tumours appear as abnormal masses of cells filling the whole lumen without clear differentiation between cells in the central area and the area located close to the basal membrane. The cell mitotic activities are visible regardless of the cell location that shows an ability to survive and grow without stromal contact. Necrotic cores are often visible inside the solid mass due to a lack of nutrients [8,20]. The corresponding computational simulations from both versions of the cell-based model are shown in figure 7a,b. In both cases the pattern is initiated in one ductal cell and each simulation ends when the duct is completely filled by tumour cells. The final configuration has been obtained by frequent proliferations of randomly chosen cells growing

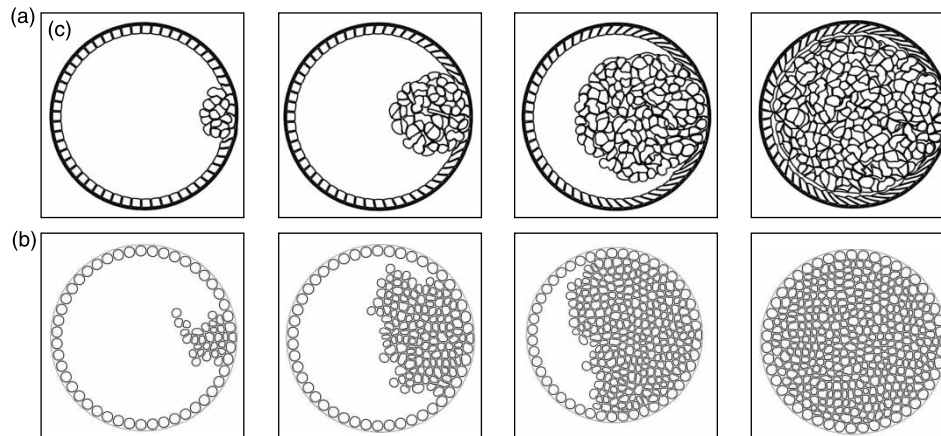


Figure 7. Development of the solid pattern initiated from one epithelial cell in the duct. Four representative snapshots from simulations of KAR (upper row) and RHD (bottom row) are shown.

equally well close to the duct as well as inside the lumen and acquiring random orientation in cell divisions. The initiation of tumour growth in a single ductal cell has been chosen to show that solid tumours have potential to fill the whole space even if they are initiated from one cell. Both presented simulations give comparable final results, even if they differ in the way the axis of cell division is determined. In the model of KAR all cells divide orthogonally to their longest axes, whereas the orientation of cell division is random in the model if RHD. This leads again to more regular boundaries of a growing cell mass in the model of KAR and to a more finger-like structure of the tumour cluster in the model of RHD.

3.5. Conclusions

Each of the presented four carcinoma patterns, micropapillary, cribriform, tufting and solid, has been independently initiated from a configuration of a normal hollow duct. The final results have been achieved by varying only two proliferative properties of the growing tumour cells: (i) the orientation of cell division, and (ii) the cell replication potential. This approach allows for comparison of all four patterns, taking into account a minimal number of features that differentiate between normal and tumoural cells. The obtained results are graphically summarized in figure 8.

Normal epithelial cells acquire only two specific planes of cell division which allows them to maintain the integrity of the epithelial tissue and cell epithelial polarisation. This condition allows for classifying cells forming four discussed patterns with regard to their epithelial vs. tumoural characteristic. The cells growing in the micropapillary patterns attain one specific orientation of cell division which depends only on their adhesive connections with other cells (low condition (i)). Similarly, the cells forming a cribriform pattern have identically defined axes of cell division despite their location within the tumour cluster (low condition (i)). In contrast, the cells forming a tufting and solid patterns exhibit lack of such cell polarity that results in more variable, even random, orientation of their mitotic axes (high condition (i)).

It is also characteristic for normal epithelial cells to carry an intrinsic program that limits the number of cell doublings to a few in the cell lifespan and after a certain number of

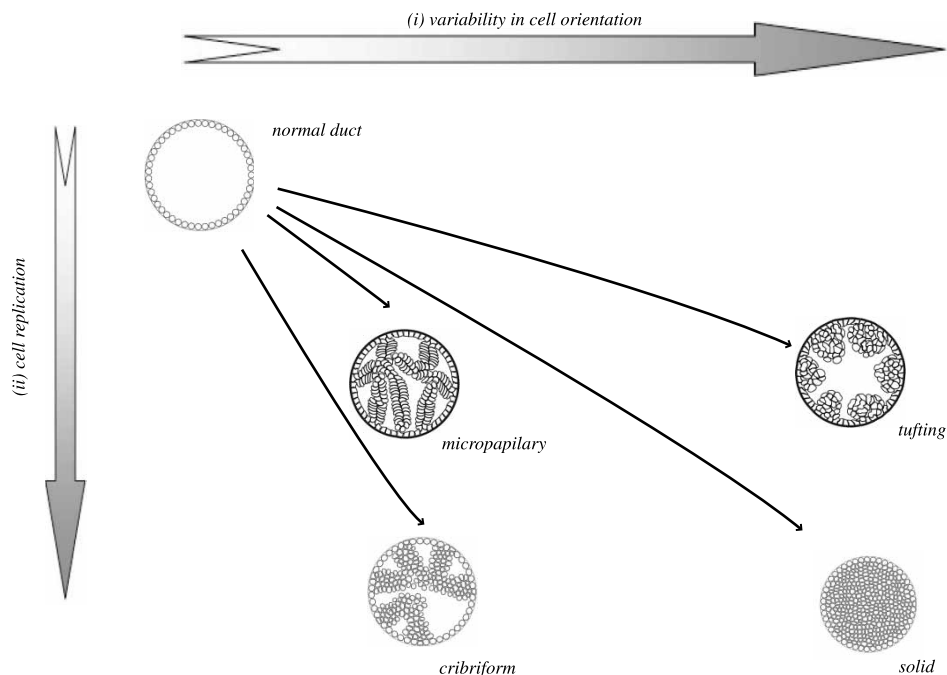


Figure 8. Gradual changes in two proliferative conditions: (i) increased variability in orientation of cell division, and (ii) increased potential of cell replication, lead to tumours of different aggressive characteristics progressing from the micropapillary to tufting and cribriform, to solid patterns.

proliferations normal cells stop growing and become senescent. The tumoural cells in the micropapillary pattern retain this epithelial characteristic quite strongly and undergo very infrequent proliferations with cell doubling limited only to one generation (low condition (ii)). The cells forming a tufting pattern exhibit limited ability for growing inside the lumen and its proliferative potential is limited to a few generations of descendants (low condition (ii)). In contrast, cells forming the cribriform and solid patterns are able to survive and grow anywhere in the lumen, without contact to the basal membrane, that reflects an increase in their malignant potential (high condition (ii)).

The simulated carcinoma patterns show increasing loss of differentiation of their precursor tumour cells when compared to the properties of normal ductal cells. The characteristic features of each pattern are summarized in table 1.

The increasing dedifferentiation of the precursor tumour cells may be an indication of the aggressive progression of the preinvasive cancers, which would suggest in turn, that the

Table 1. Final characteristics of four simulated carcinoma patterns.

Cell pattern	Cell growth	Cell orientation	Final characteristics
Micropapillary	Reduced	Fixed	Epithelial
Tufting	Reduced	Random	Intermediate
Cribriform	Unbounded	Fixed	Intermediate
Solid	Unbounded	Random	Tumoural

aggressive characteristics among four simulated tumours progresses from the micropapillary to cribriform and tufting, and finally to solid patterns. The tufting and cribriform patterns have been classified together to be of intermediate aggressive characteristics; however, each of them has scored differently in our two-factor grading system. The tufting pattern has gained its position due to the lack of cell polarisation and to random orientation of cell divisions, whereas the cribriform pattern due to its potential of unlimited cell proliferation. At this point these two microarchitectures are incomparable and the third condition may be needed to find which of these two carcinomas is relatively more aggressive.

4. Discussion

We presented in this paper a single cell-based mathematical model that is able to simulate the formation of distinct cell patterns observed in histological biopsy samples from ductal carcinomas *in situ* of human breast and prostate. The final results showing the development of solid, tufting, cribriform and micropapillary microarchitectures have been obtained by varying only two proliferative properties of the precursor cells: their replicable potential and the variability in orientation of cell division. This allowed for comparison of all four patterns taking into account a minimal number of features that differentiate between epithelial and tumoural cells. The obtained results suggest that the aggressive characteristics among four discussed tumours progress from the micropapillary to cribriform and tufting, to solid patterns; however, further experimental studies will be needed to validate our hypotheses regarding a degree of epithelial polarisation of the growing tumour cells, the orientation of cell divisions and the localization of mitotic events during the development of discussed carcinoma patterns.

We do not claim here that one carcinoma pattern can evolve into another, but that there are certain mutations independently appearing in the precursor tumoural cells that give rise to each of the discussed patterns separately. However, as consequence of those mutations, the precursor tumour cells and the resulting carcinoma patterns can be ordered according to their aggressive properties. This is consistent with biological observations that each of the different ductal carcinoma has the potential to progress to an invasive phenotype. However, there is also no biological evidence to support progression from one lower-grade ductal carcinoma to the higher-grade DCIS through intermediate grades [19].

Future extensions of this mathematical model may incorporate some external factors and biochemical processes that will help in building further hypotheses. For instance, it is not known why tufting patterns reach only a few layers in width and what causes their growth suppression. It may be a result of the lack of nutrients or growth factors inside the duct, and we plan to investigate in our further work what conditions can lead to such situation. Similarly, it is not clear how the multilumens in the cribriform carcinomas are maintained and why they appear to be of regular, roundish shapes. This also will be a subject of our future work. In all our simulations the tumour growth was initiated in preselected cells, since we focused on the properties of cell growth and division; however, it should be also investigated what external conditions (nutrients, growth factors and tissue pressure) can lead to quite uniform spacing of intraductal patterns observed in some real carcinomas.

It is not known how the DCIS that grows inside a duct can influence changes in the size and structure of the host duct, and whether the pressure from the growing tumour cells can lead to the duct deformation. We plan to address these questions in our future work. Another issue

not considered in this paper is cell death. However, in future work we plan to include different types of cell death (necrotic, apoptotic and anoikis) and investigate their influence on different patterns of intraductal tumours.

Acknowledgements

The work of RHD has been supported by the National Science Foundation grants DMS0109957 and DMS0201063. The work of KAR has been supported partially by the Mathematical Biosciences Institute at the Ohio State University under agreement no. 0112050 with the U.S. National Science Foundation.

References

- [1] Bostwick, D.G., Amin, M.B., Dundore, P., Marsh, W. and Schultz, D.S., 1993, Architectural patterns of high-grade prostatic intraepithelial neoplasia, *Human Pathology*, **24**, 298–310.
- [2] Che, M. and Grignon, D., 2002, Pathology of prostate cancer, *Cancer and Metastasis Reviews*, **21**, 381–395.
- [3] Debnath, J. and Brugge, J.S., 2005, Modelling glandular epithelial cancers in three-dimensional cultures, *Nature Reviews Cancer*, **5**, 675–688.
- [4] Dillon, R. and Othmer, H., 1999, A mathematical model for outgrowth and spatial patterning of the vertebrate limb bud, *Journal of Theoretical Biology*, **197**, 295–330.
- [5] Dillon, R.H., Owen, M. and Painter, K., An immersed boundary model of multicellular growth, in preparation.
- [6] Ferguson, D.J.P., 1985, Ultrastructural characterisation of the proliferative (stem?) cells within the parenchyma of the normal “resting” breast, *Virchows Archiv [Pathological Anatomy]*, **407**, 379–385.
- [7] Ferguson, D.J.P., 1988, An ultrastructural study of mitosis and cytokinesis in normal “resting” human breast, *Cell and Tissue Research*, **252**, 581–587.
- [8] Fischer, A., How breast cancer is diagnosed, <http://mammary.nih.gov/reviews/tumorigenesis/Fischer001/slides/intropg2.htm>
- [9] Mallon, E., Osin, P., Nasiri, N., Blain, I., Howard, B. and Gusterson, B., 2000, The basic pathology of human breast cancer, *Journal of Mammary Gland Biology and Neoplasia*, **5**, 139–163.
- [10] Nelson, C.M. and Bissell, M., 2005, Modeling dynamics reciprocity: engineering three-dimensional culture models of breast architecture, function and neoplastic transformation, *Seminars in Cancer Biology*, **15**, 342–352.
- [11] O’Brien, L.E., Zegers, M.M.P. and Mostov, K.E., 2002, Building epithelial architecture: insights from three-dimensional culture models, *Nature Reviews Molecular Cell Biology*, **3**, 531–537.
- [12] Park, J.-H., Walls, J.E., Galvez, J.J., Kim, M., Abate-Shen, C., Shen, M.M. and Cardiff, R.D., 2002, Prostatic intraepithelial neoplasia in genetically engineered mice, *American Journal of Pathology*, **161**, 727–735.
- [13] Peskin, C., 2002, The immersed boundary method, *Acta Numerica*, **11**, 479–517.
- [14] Rejniak, K.A., Kliman, H.J. and Fauci, L.J., 2004, A computational model of the mechanics of growth of the villous trophoblast bilayer, *Bulletin of Mathematical Biology*, **66**, 199–232.
- [15] Rejniak, K.A., 2005, A single-cell approach in modeling the dynamics of tumor microregions, *Mathematical Biosciences and Engineering*, **2**(3), 643–655.
- [16] Rejniak, K.A., An immersed boundary framework for modelling the growth of individual cells: an application to the early tumour development, *Journal of Theoretical Biology*, in print, <http://dx.doi.org/10.1016/j.jtbi.2007.02.019>.
- [17] Schulze-Garg, C., Löhler, J., Gocht, A. and Deppert, W., 2000, A transgenic mouse model for the ductal carcinoma *in situ* (DCIS) of the mammary gland, *Oncogene*, **19**, 1028–1037.
- [18] Straight, S.W., Shin, K., Fogg, V.C., Fan, S., Liu, C.-J., Roh, M. and Margolis, B., 2004, Loss of PALS1 expression leads to tight junction and polarity defects, *Molecular Biology*, **15**, 1981–1990.
- [19] Tavassoli, F.A., 2001, Ductal intraepithelial neoplasia of the breast, *Virchows Archiv*, **438**, 221–227.
- [20] Winchester, D.P., Jeske, J.M. and Goldschmidt, R.A., 2000, The diagnosis and management of ductal carcinoma *in-situ* of the breast, *Cancer Journal for Clinicians*, **50**, 184–200.
- [21] Laurent, V.M., Planus, E., Fodil, R. and Isabey, D., 2003, Mechanical assessment by magnocytometry of the cytosolic and cortical cytoskeletal compartments in adherent epithelial cells, *Biorheology*, **40**, 235–240.
- [22] Dembo, M. and Harlow, F., 1986, Cell motion, contractile networks, and the physics of interpenetrating reactive flow, *Biophysics Journal*, **50**, 109–121.
- [23] Park, A., Koch, D., Cardenas, R., Kas, J. and Shih, C.K., 2005, Cell motility and local viscosity of fibroblasts, *Biophysics Journal*, **89**, 4330–4342.
- [24] Bell, G.I., 1978, Models for specific adhesion of cells to cells, *Science*, **200**, 618–627.

- [25] Mathur, A.B., Truskey, G.A. and Reichert, W.M., 2000, Atomic force and total internal reflection fluorescence microscopy for the study of force transmission in endothelial cell, *Biophysical Journal*, **78**, 1725–1735.
- [26] Baumgartner, W. and Drenckhahn, D., 2002, Transmembrane cooperative linkage in cellular adhesion, *European Journal of Cell Biology*, **81**, 161–168.

A. Appendix

We have presented in section 2 an outline of the mathematical model of a growing viscoelastic cell based on the immersed boundary method. In this section, we discuss details of two implementations of this mathematical framework. The methods used by KAR and by RHD are similar in concept but vary in some details of the structure of cell membranes, in the distribution of sources and sinks of fluid in the growing cells, and in determining the axis of cell division. Some of the numerical and biophysical parameters used in both implementations differ in their values. The model implemented by KAR was used to simulate the micropapillary, tufting and solid patterns, figures 4, 6a and 7a, respectively. The model implemented by RHD was used to simulate the cribriform, tufting and solid patterns, figures 5, 6b and 7b, respectively. Both implementations produce comparable final results. This shows the validity of the general mathematical framework in modelling the growth of multicellular tissues, but also indicates that some degree of freedom is allowed in defining particular elements of the model. In this section, we discuss differences between our two model implementations. More detail on each model separately can be found in Refs [5] (RHD) and [16] (KAR).

A.1 Structure of the cell membrane

Each cell in both models is represented by a discrete collection of Lagrangian points $\{\mathbf{X}_l(t)\}$ that form the elastic plasma membrane enclosing the fluid cytoplasm. The elasticity of cell membranes comes from linear springs \mathbf{F}_{adj} acting on two distinct boundary points \mathbf{X}_l and \mathbf{X}_m , and satisfying Hooke's law with the constant resting length \mathcal{L}_{adj} and constant spring stiffness \mathcal{F}_{adj} ,

$$\mathbf{F}_{\text{adj}}(l, t) = \mathcal{F}_{\text{adj}} \frac{\|\mathbf{X}_m(t) - \mathbf{X}_l(t)\| - \mathcal{L}_{\text{adj}}}{\|\mathbf{X}_m(t) - \mathbf{X}_l(t)\|} (\mathbf{X}_m(t) - \mathbf{X}_l(t)). \quad (\text{A1})$$

The model of cell membrane used by KAR consists of a collection of points forming one closed curve, where each boundary point is connected to its four neighbours (two on each side) by linear springs of the form given in equation (A1). The model of cell membrane used by RHD consists of a collection of points forming two closed curves, where each boundary point is connected to its two neighbours on the same curve and three neighbours on the other curve to form a crossed network. Each connection is defined by a linear spring of the form given in equation (A1). Both models are presented in figure A1a,b, respectively.

A.2 Contractile forces and the axis of cell division

The contractile forces are introduced in the cell that has doubled its area and is ready to split into two daughter cells. In both implementations the contractile ring has a form of three links that extend across the cell, figure A1a,b. In the model used by RHD the common direction of these three links is chosen either randomly or orthogonal to the line running from the cell

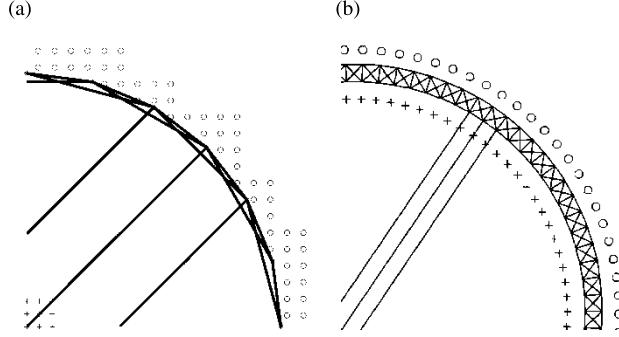


Figure A1. Schematic representation of a part of the cell from the model implementation by: (a) KAR, and (b) RHD. The cell wall is represented as a single closed curve where each boundary point is connected to its four neighbours, two on each side (model a) or as a mesh of linear elastic forces on two closed curves (model b). The transport of fluid from the exterior to the interior is modelled by placing fluid sources (+) and sinks (O) in the growing cell—in the form of a discrete neighbourhood (model a) or in the form of discrete channels (model b). The contractile links extend across the cell—three solid lines in both models. Note, that the boundary points in model (a) are placed very sparsely for clarity of the presentation.

centroid to the closest point on the basal membrane. In the model used by KAR the common direction of three contractile links is either orthogonal to the cell longest axis or orthogonal to the cell boundary that adheres to other cells. Once the orientation of contractile links is determined, the contractile forces \mathbf{F}_{div} act on the cell boundaries until the opposite points $\mathbf{X}_l(t)$ and $\mathbf{X}_k(t)$ reach a distance $\mathcal{L}_{\text{div}}^{\text{min}}$, at which point the dividing cell splits into two daughter cells. Each contractile force satisfies Hooke's law with the constant resting length \mathcal{L}_{div} and constant spring stiffness \mathcal{F}_{div} :

$$\mathbf{F}_{\text{div}}(l, t) = \mathcal{F}_{\text{div}} \frac{\|\mathbf{X}_k(t) - \mathbf{X}_l(t)\| - \mathcal{L}_{\text{div}}}{\|\mathbf{X}_k(t) - \mathbf{X}_l(t)\|} (\mathbf{X}_k(t) - \mathbf{X}_l(t)), \quad (\text{A2})$$

provided $\|\mathbf{X}_l(t) - \mathbf{X}_k(t)\| \geq \mathcal{L}_{\text{div}}^{\text{min}}$ and is zero otherwise.

A.3 Source-sink distribution

The distribution of sources and sinks used to model transport of the fluid through the membranes of growing cells is modelled differently in both implementations. In the model by KAR the sources of fluid are located at the cell centres and the balancing sinks are placed in the discrete neighbourhood outside the boundaries of each growing cell, Figure A1a. The strength of each fluid source $S^+(\mathbf{Y}_k^+, t)$ is a step function that takes a nonzero value over the time of cell growth, but once the cell area is doubled, the fluid sources are deactivated. In this model the number of balancing sinks can be different than the number of sources, thus the strength of each sink is determined to balance the total source strength for all growing cells. In the model by RHD the sources and sinks of fluid are placed along the cell boundary in the form of discrete channels (Figure A1b). The number of sources and sinks defined for the same cell are equal and their strengths are taken to have opposite values.

Figure A1a,b shows the structure of a part of a single eukaryotic cell from both discussed implementations. In particular it includes the structure of the cell membrane, location of the contractile ring and location of fluid sources and sinks.

A.4 Structure of the basal membrane

The basal membrane in both models is represented by a discrete collection of Lagrangian points $\{\mathbf{Z}_l(t)\}$ that form one closed curve (model by RHD) or two closed curves (model of KAR). Each boundary point is connected to its two neighbours on the same curve. Additionally in the model by KAR, each boundary point is connected to two neighbouring points on the other curve to form a crossed network. Each connection is modelled by a linear spring \mathbf{F}_{adj} that acts on two distinct boundary points \mathbf{Z}_l and \mathbf{Z}_m , and satisfies Hooke's law with the constant resting length \mathcal{L}_{adj} and constant spring stiffness \mathcal{F}_{adj} :

$$\mathbf{F}_{\text{adj}}(l, t) = \mathcal{F}_{\text{adj}} \frac{\|\mathbf{Z}_m(t) - \mathbf{Z}_l(t)\| - \mathcal{L}_{\text{adj}}}{\|\mathbf{Z}_m(t) - \mathbf{Z}_l(t)\|} (\mathbf{Z}_m(t) - \mathbf{Z}_l(t)). \quad (\text{A3})$$

In both implementations we introduce additional tethered forces that act in each boundary point $\mathbf{Z}_m(t)$ and have the following form:

$$\mathbf{F}_{\text{th}}(l, t) = \mathcal{F}_{\text{th}} (\mathbf{Z}_m(t) - \mathbf{Z}_m^l(t)). \quad (\text{A4})$$

where \mathcal{F}_{th} is a constant spring stiffness and $\mathbf{Z}_m^l(t)$ is the initial location of the boundary point $\mathbf{Z}_m(t)$.

A.5 Adherent connections

Separate cells in the tissue can adhere to their neighbours and these adherent links are represented as short linear springs attached at the boundary points $\mathbf{X}_i(t)$ and $\mathbf{X}_k(t)$ of two distinct cells if they are within the predefined distance $\mathcal{L}_{\text{adh}}^{\text{max}}$. The adhesive force \mathbf{F}_{adh} satisfies Hooke's law with the constant resting length \mathcal{L}_{adh} and constant spring stiffness \mathcal{F}_{adh} :

$$\mathbf{F}_{\text{adh}}(l, t) = \mathcal{F}_{\text{adh}} \frac{\|\mathbf{X}_k(t) - \mathbf{X}_l(t)\| - \mathcal{L}_{\text{adh}}}{\|\mathbf{X}_k(t) - \mathbf{X}_l(t)\|} (\mathbf{X}_k(t) - \mathbf{X}_l(t)), \quad (\text{A5})$$

provided $\|\mathbf{X}_k(t) - \mathbf{X}_l(t)\| \leq \mathcal{L}_{\text{adh}}^{\text{max}}$ and is zero otherwise. Note that this equation also represents a repulsive force if the distance between cell boundaries is smaller than \mathcal{L}_{adh} . Cells located along the duct can also develop adherent connections with the basal membrane and these adherent connections are defined in the very similar way.

Figure A2a,b shows the structure of the basal membrane and adhesion links between separate cells and between cells and the basal membrane from both discussed implementations.

A.6 Comments

The two implementations of the cell-based model presented here use the same general principles of the immersed boundary method. The cells are modelled as elastic bodies immersed in the viscous incompressible fluid and its motion is influenced by various forces acting on the boundaries of all cells and by sources and sinks of fluid used to model cell growth. Both implementations differ in the design of structure of the cell membrane, in the location of sources and sinks of the fluid in the growing cells, and in the algorithms for selection of the orientation of cell division. However, they produce comparable results, that show the potential of our single cell-based technique in modelling various patterns of the

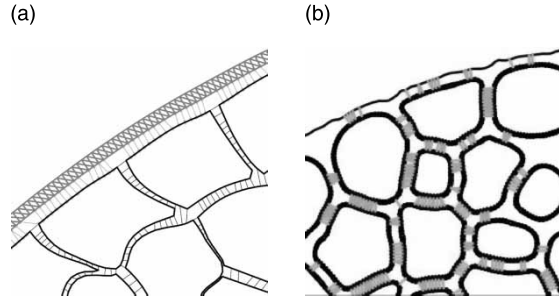


Figure A2. Schematic representation of the basal membrane and the adhesive connections between separate cells and between ductal cells and the basal membrane in the model implementation by: (a) KAR, and (b) RHD.

multicellular growth, simultaneously giving the modeller a certain degree of freedom in defining some model details.

The parameter values used in both implementations vary. However, no experimental measurements of biophysical data are presently available for *in vivo* formation of ductal carcinomas. Moreover, even if tumour cells in each pattern have similar origin in ductal epithelium, their physical properties, such as cell stiffness or adhesiveness to other cells, may significantly vary among different tumour cell lines. We have simplified our approach here by using the same biophysical parameters for all carcinomas because our goal was to focus on individual cell processes and on the relations between cells rather than on matching specific biophysical parameters, that may depend strongly on experimental methodology, cell line, and whether the host cells are cultured or extracted from living tissues. The model

Table A1. Biophysical parameters used in both model implementations and reported in the literature.

Physical parameter		KAR model	RHD model	Comments and references
Cell diameter	$d_{\text{cell}} =$	10 μm	9 μm	10–20 μm [8]
Duct diameter	$d_{\text{duct}} =$	225 μm	180 μm	150 μm –1 mm [8]
Fluid viscosity	$\mu =$	100 g/(cm s)	1000 g/(cm s)	50–140 g/(cm s) cortical cytoplasm [21] 10 ² –10 ⁶ g/(cm s) network cytoplasm [22]
Fluid density	$\rho =$	1.35 g/cm ³	1.0 g/cm ³	1.35 g/cm ³ network cytoplasm [22] 1.1 g/cm ³ aqueous cytoplasm [22]
Source strength	$S^+ =$	2×10^{-7} g/cm	2×10^{-5} g/cm	Determined computationally
Force stiffness Adjacent	$\mathcal{F}_{\text{adj}} =$	500 g/(cm s ²)	8×10^4 g/(cm \times s ²)	490–850 g/(cm s ²) epithelial elasticity [21] 0.42–1.4 $\times 10^4$ g/(cm s ²) fibroblast elasticity [23] 2.18–3.76 $\times 10^4$ g/(cm s ²) endothelial elasticity [25]
Adherent-repulsive	$\mathcal{F}_{\text{adh}} =$	100 g/(cm s ²)	5×10^4 g/(cm s ²)	10 ³ g/cm s ² normal cells separation [24] 0.1–10 ³ g/(cm s ²) cell-substrate detachment [26]
Contractile	$\mathcal{F}_{\text{div}} =$	5×10^7 g/(cm s ²)	4×10^4 g/(cm s ²)	0–10 ⁶ g/(cm s ²) contractile stress [22]

may be, however, revisited when the value of real parameters will be available. Similarly, due to the lack of experimental models that would be able to trace the development of ductal carcinomas, there is no information available about the period of time over which the particular *in vivo* patterns are formed. Therefore, we were not aiming here to match the real time of pattern formation. Table A1 contains values of biophysical parameters used in each implementation and real parameters as reported in the literature.